Journal of Building Engineering 98 (2024) 111252

Contents lists available at ScienceDirect

Journal of Building Engineering

journal homepage: www.elsevier.com/locate/jobe

Extrudability analysis of 3D printable concrete as a two-phase discrete flow

Yubo Sun [a], Xinyue Zhang [b], Jiangang Zhou [c], Yilin Wang [d], Bo Zhang [d], Yiyuan Zhang [d], Weijiu Cui [e,**], Yaxin Tao [f,*]

[a] Department of Civil and Environmental Engineering, Hong Kong Polytechnic University, Hong Kong, China
[b] Department of Architectural Engineering, Binzhou Polytechnic, Binzhou, China
[c] Architectural Engineering Institute, Weifang Engineering Vocational College, Weifang, China
[d] Department of Structural Engineering and Building Materials, Ghent University, Ghent, Belgium
[e] Department of Civil Engineering, Qingdao University of Technology, Qingdao, China
[f] Institute of Building Materials, ETH Zurich, Zurich, Switzerland

ARTICLE INFO

Keywords:
3D concrete printing
Extrudability
Clogging
Two-phase discrete element method
Printing nozzle optimization

ABSTRACT

3D printing with concrete is primarily achieved through an extrusion process, where the material is precisely deposited layer by layer to construct structures. Proper control of extrusion ensures consistent material flow, accurate layer formation, and the overall stability of the 3D-printed structure. However, clogging during the extrusion process can occur as the nozzle size is too small relative to the aggregate size. To fundamentally understand the clogging mechanism and optimize the extrusion process, a precise two-phase discrete element model was established to simulate the extrusion process. A cluster of particles was used to model fresh concrete, with hard cores representing the aggregates and concentric soft shells representing fresh cement paste surrounding them. Five nozzles with different outlet diameters were designed and 3D printable concrete with different fineness modulus levels was formulated. The parameters of the two-phase discrete element model were determined based on rheological properties and calibrated using slump flow test results. The simulation results showed good agreement with the experimental pressure values and the quality of extruded filaments. Based on these results, it suggested that ensuring a proper balance between the aggregate fineness modulus and the outlet diameter of printing nozzles is essential for the extrusion process.

1. Introduction

In the realm of modern construction, the advent of 3D printing technology has introduced revolutionary changes. 3D concrete printing, a subset of additive manufacturing, allows for the creation of complex, large-scale structures with enhanced efficiency, reduced waste, and unprecedented design flexibility [1–3]. Unlike traditional concrete casting methods, which rely on molds to shape the material, 3D concrete printing extrudes a specially formulated concrete mixture layer by layer, constructing the desired structure without the need for formwork [4]. This innovative approach is transforming the construction industry, paving the way for faster, more

* Corresponding author.
** Corresponding author.
E-mail addresses: cuiweijiu@163.com (W. Cui), yaxtao@ethz.ch (Y. Tao).

https://doi.org/10.1016/j.jobe.2024.111252
Received 24 August 2024; Received in revised form 3 October 2024; Accepted 4 November 2024
Available online 5 November 2024
2352-7102/© 2024 The Authors. Published by Elsevier Ltd. This is an open access article under the CC BY license (http://creativecommons.org/licenses/by/4.0/).

sustainable, and cost-effective building processes.

The transition from conventional mold-cast concrete to 3D printable concrete still faces its challenges. Traditional mold-cast concrete can utilize a wide range of aggregate sizes and compositions, as the concrete is simply poured into a form where it hardens. In contrast, pumpable concrete requires a finer balance, as the mixture must be fluid enough to be pumped through hoses and pipes but also robust enough to retain its integrity once placed. This need for pumpability led to the development of concrete mixtures with modified aggregate content and the use of various admixtures to enhance flowability [5,6]. With the advent of 3D concrete printing, the requirements became even more stringent. The concrete must be not only pumpable but also extrudable, which means it must possess a unique combination of flow properties, setting characteristics, and structural stability [7–11]. The aggregate content must be carefully controlled to ensure that the mixture can be extruded through the narrow nozzle of the printer without clogging.

Clogging is one of the most critical challenges encountered during the extrusion process of 3D printable concrete. It occurs when the concrete mixture becomes obstructed, preventing the smooth flow of material and leading to interruptions in the printing process. Clogging can be caused by several factors, including the large particle size, the high content of the aggregates, the high viscosity of the mixture, and the strong interaction between the components of the concrete [12]. One of the primary reasons for clogging is the presence of oversized particles or an excessive concentration of particles within the concrete mixture [13,14]. In traditional concrete, larger aggregates contribute to the material's strength and stability. However, in the context of 3D printing, these larger particles can obstruct the narrow pathways within the pump and nozzle, leading to blockages [15]. As the particle size increases, the likelihood of particles getting stuck in the system also increases, especially in sections where the flow path narrows or changes direction. Similarly, increasing the aggregate content, even if the particles are within the acceptable size range, can also lead to clogging [5]. A high concentration of particles in the mixture can cause them to cluster together, forming agglomerates that are too large to pass through the nozzle. These clusters can become trapped within the system, leading to a buildup of pressure and eventually causing a blockage. In addition to particle size and content, other factors can contribute to clogging. The interaction between the aggregates and the cement paste can play a significant role in the mixture's flowability [16]. If the paste is too viscous or if the particle-paste interaction is too strong, the mixture may become too thick to pump or extrude effectively. This can lead to increased resistance within the system, causing the mixture to slow down or stop entirely, resulting in a clog. Although the innovative approach of quick nozzle mixing by Zhang et al. [17], where the material is mixed directly within the nozzle, offers the potential for reducing the risk of clogging, this method may still encounter challenges, particularly due to the rapid setting of the material. Consequently, a detailed clogging analysis remains essential to fully address these issues and ensure consistent material flow during the extrusion process.

Given the complexities involved in understanding extrudability and preventing clogging in 3D concrete printing, experimental approaches can be time-consuming and resource-intensive. Experimentally testing each variation in concrete composition to assess its susceptibility to clogging requires significant effort. This process must be repeated for each potential formulation, making it an impractical approach for optimizing 3D printable concrete. To address this challenge, simulation techniques have emerged as a powerful tool for clogging analysis. By using computational models to simulate the flow of concrete through the extrusion system, researchers can predict the clogging under different models. Various approaches have been developed. Computational fluid dynamics (CFD) can model the fluid-like behavior of concrete but often struggles with accurately capturing the interaction between solid aggregates and the cement paste [18–20]. Yu et al. [21] introduced an innovative application of Smoothed Particle Hydrodynamics (SPH) to numerically estimate the geometrical quality of the extruded filament. However, their study did not address the occurrence of clogging during the extrusion process. The discrete element method (DEM) alone fails to account for the effects of the cement paste [22]. Although coupling CFD with DEM provides a more comprehensive approach, it introduces significant computational and modeling complexities, making it difficult to apply effectively [23,24]. To address these issues, recent research has introduced models that treat aggregate particles as having a rigid core with a soft shell representing the cement paste. This approach offers a balanced solution, capturing both the particle interactions and the flow behavior of the paste with greater accuracy and less computational burden. Some studies using the two-phase discrete element method have been carried out to simulate the flow behavior of concrete. For example, Remond and Pizette [25] carried out two kinds of simulations using the hard-core and soft-shell model, including rheological simulations performed in a Couette geometry and slump test simulations, and the flow behavior of concrete was well-predicted. Mechtcherine et al. [26] made use of the two-phase model to predict the flow of fresh concrete through slump flow and LCPC-box tests, and the model provided satisfactory predicting results. In addition, A hard-core soft-shell model of fresh concrete under different vibration conditions was created, following the same modeling procedure by Li et al. [27]. Within the scope of 3D concrete printing, Ramyar et al. [28] proposed the discrete fresh concrete model, where the interaction among coarse aggregate particles embedded in a fine mortar was modeled using stress-strain constitutive equations, with parameters that have well-defined physical significance. Unfortunately, so far, there has been a notable lack of research specifically focusing on extrudability analysis during the 3D concrete printing process as influenced by aggregates and outlet dimensions.

In this paper, we investigated the extrudability of 3D printable concrete and employed a combination of experimental and simulation approaches. We began by developing a two-phase discrete element model to simulate the flow of concrete. The concrete was modeled as a composite material composed of two distinct phases, including a rigid core representing the solid aggregate particles and a soft outer layer simulating the surrounding cement paste. The slump test was used to calibrate the numerical model, and extrusion simulation was carried out. In parallel, we conducted a series of experiments to test different concrete mixtures with different fineness moduli under controlled conditions, measuring the pressure and morphology of the material as it passed through an extrusion setup with different outlet diameters. Finally, the numerical and experimental results were compared.

2. Experimental program

2.1. Materials and mixture design

The cement used was a fast-hardening P42.5 grade, produced by Wuxi Jianghuai Building Materials Technology Co., Ltd., with supplementary cementitious materials added to reduce the cement content. Specifically, silica fume, secondary-grade fly ash, and ground granulated blast furnace slag were sourced from Henan Borun Casting Materials Co., Ltd. Manufactured sand with a maximum aggregate size of 4.75 mm was provided by Qingdao Construction Company, with three different fineness moduli including 2.5, 2.9, and 3.3. The particle size distribution of manufactured sand is shown in Fig. 1. The study utilized hydroxypropyl methylcellulose (HPMC) ether, with a viscosity of 4000 P · s, and a polycarboxylate superplasticizer with a water reduction rate of 27 %, supplied by Shanxi Feike New Materials Technology Co., Ltd.

The binder system consisted of 50 % cement, 15 % fly ash, 30 % GGBS, and 5 % silica fume, with a water-binder ratio of 0.35 and a sand-to-binder ratio of 1.25. The selection of fly ash, GGBS, and silica fume is based on their well-documented performance as supplementary cementitious materials (SCMs). The specific proportions of these materials are derived from previous research by the authors [29], which demonstrated their effectiveness in optimizing the rheological and mechanical behavior of concrete mixtures, particularly in the context of extrusion processes for 3D concrete printing. The cellulose ether dosage was fixed at 0.2 % by the mass of the binder, and the superplasticizer dosage was 0.05 % by the mass of the binder.

2.2. Slump and slump flow tests

The slump and slump flow tests were conducted to assess the workability of the concrete mixtures, following the standard ASTM C143-90 (Standard test method for slump of hydraulic cement concrete, American Society for Testing and Materials). For the slump test, a standard slump cone was placed on a flat, moist, and non-absorbent surface. The cone was filled with concrete in three equal layers, each tamped 25 times with a tamping rod to remove air pockets. After the cone was filled, it was carefully lifted vertically, allowing the concrete to slump. The vertical distance between the top of the cone and the highest point of the slumped concrete was measured as the slump value. For the slump flow test, the same procedure was followed, but after lifting the cone, the diameter of the spread concrete was measured in two perpendicular directions. The average of these two measurements was recorded as the slump flow value. The test was repeated twice for each series.

2.3. Rheological tests

Two kinds of rheological tests were conducted, including stress growth tests and flow curve tests. The stress growth test was conducted using the Schleibinger eBT-V concrete rheometer to evaluate the static yield stress. First, the prepared concrete sample was loaded into the rheometer's measuring cell (diameter 244 mm, volume 20 L). After that, the rheometer was set to stress growth mode. A constant rotational speed (0.5 rpm) was applied starting from a stationary state. The test continued for a total period of 180 s. The maximum value of shear stress, i.e., static yield stress, was calculated from the peak torque value [30].

Following the stress growth test, the flow curve measurements were conducted to assess the dynamic yield stress and plastic viscosity. The rheometer was reset and switched to flow curve mode, which consisted of a pre-shearing stage and a testing stage. During the pre-shearing stage, the rotational speed was set constantly at 30 rpm for 20 s. After that, the testing stage was divided into

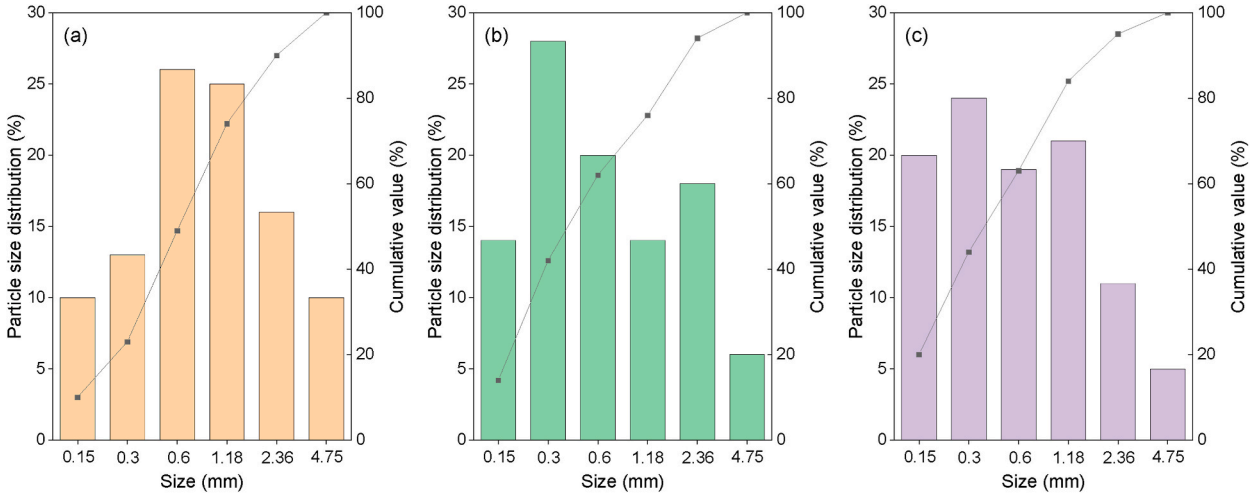

Fig. 1. Particle size distribution of manufactured sand with different fineness moduli: (a) fine modulus 3.3, (b) fine modulus 2.9, and (c) fine modulus 2.5.

six stages, with each stage lasting 10 s. The initial stage was set to a maximum rotational speed of 25.5 rpm, followed by a gradual decrease in speed for each subsequent stage. The final stage was conducted at a rotational speed of 3 rpm. More details about the calculation of rheological properties can be found in previous studies [31].

2.4. Extrusion tests

The 3D printing setup used in this study consists of a piston device powered by an electric motor, specifically designed to extrude concrete materials. The inner diameter and the length of the piston are 50 and 300 mm, respectively. The extrusion rate was set at 20 mm/s. A load cell with a capacity of 2 kN was attached to the upper part of the piston to monitor the force exerted during the extrusion process. Data from the extrusion process, including time and force, were recorded using the Autoda Test data acquisition system. For each test group, data collection was conducted for 60 s, with a sampling interval of 100 ms, resulting in 600 pressure data points per group. The extruded material was deposited onto a roller band measuring 200 mm in width and 750 mm in length. The conveyor moved at a speed of 5 mm/s, and the distance between the nozzle and the conveyor belt was maintained at 10 mm, as shown in Fig. 2 (a). Extrusion nozzles of different outlet diameters, including 15, 20, 25, 30, and 35 mm, were used, as shown in Fig. 2 (b). The diameter of the material loading cylinder above the nozzle was 50 mm. To reduce the effect of the dead zone at the nozzle position during extrusion, the cone angle was set at 45 °. The ratio of the nozzle diameter to the maximum aggregate size, referred to as "a", was ranged from 3 to 7, as detailed in Table 1.

Each set of experiments involved three extrusions, with each extrusion forming a single filament of concrete. For each test, a filament was extruded to a length of 300 mm. Photographs of the filaments were taken from the top view to analyze the geometric properties and consistency of the extruded material.

3. Two-phase model formulation

3.1. Kinematic equations

The Particle Flow Code (PFC, version 5.0), developed by ITASCA Consultants GmbH Ecully (France), served as the primary simulation tool for this study. In this software, each computational cycle is composed of two primary steps. First, the equations of motion are applied to all two-phase particles to determine their new positions. Next, the constitutive law is applied at each contact point to compute the forces. Contacts, whether between particles or between a particle and a wall, are automatically detected based on the distance and occur at a single point at any given moment.

The contact force updates adhere to Newton's second law. $\boldsymbol{F}_i$ denotes the force exerted by particle A on particle B during contact, or by a particle on a wall during interaction, as schematically shown in Fig. 3. These forces decompose into the normal component $\boldsymbol{F}_i^n$ and the shear component $\boldsymbol{F}_i^s$, governed by Eq. (1):

$$\boldsymbol{F}_i = \boldsymbol{F}_i^n + \boldsymbol{F}_i^s \tag{1}$$

The force-displacement law connects these force components to the respective components of relative displacement through the normal and shear stiffness at the contact point, which is detailed in Eq. (2):

$$\boldsymbol{F}_i = k^n \cdot U^n \cdot \boldsymbol{n}_i + k^s \cdot \Delta U_i^s \cdot \boldsymbol{n}_s \tag{2}$$

where k^n is the normal stiffness, U^n is the normal overlap between two particles, or between a particle and a wall, $\boldsymbol{n}_i$ represents the unit normal vector of the contact plane, k^s is the tangential contact stiffness, and ΔU_i^s represents the tangential relative displacement of the particle, $\boldsymbol{n}_s$ represents the unit tangential vector.

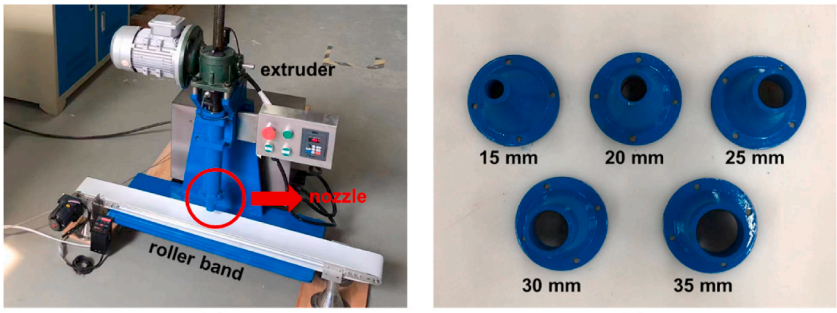

Fig. 2. Extrusion setup: (a) whole setup consisting of a piston and a roller band, (b) extrusion nozzles with different outlet diameters.

Table 1
Combinations of different mixture designs and nozzle diameters.

No.	Fineness modulus	Nozzle outlet diameter (mm)	Ratio "a"
M1-D3	3.3	15	3
M1-D4	3.3	20	4
M1-D5	3.3	25	5
M1-D6	3.3	30	6
M1-D7	3.3	35	7
M2-D3	2.9	15	3
M2-D4	2.9	20	4
M2-D5	2.9	25	5
M2-D6	2.9	30	6
M2-D7	2.9	35	7
M3-D3	2.5	15	3
M3-D4	2.5	20	4
M3-D5	2.5	25	5
M3-D6	2.5	30	6
M3-D7	2.5	35	7

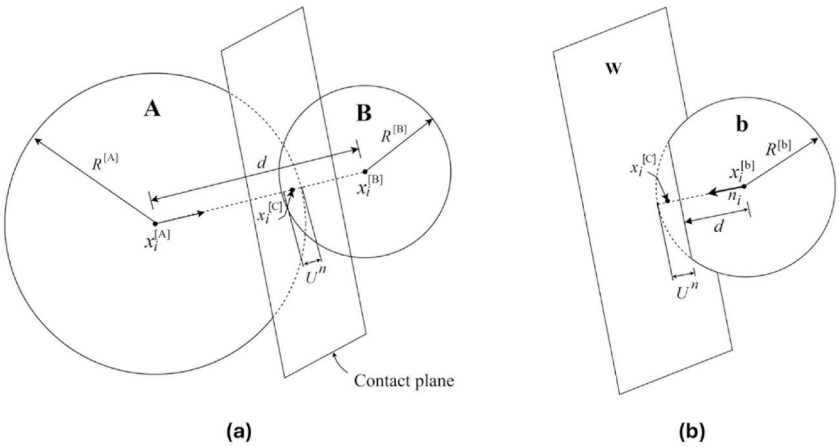

Fig. 3. Schematic of two-phase discrete element model: (a) contact between particles, and (b) contact between wall and particle.

3.2. Constitutive law

In the model, fresh concrete is considered as a cluster of particles with a hard core and a soft shell. The hard core symbolizes the large-size aggregate in concrete, characterized by a radius $R_{i,j}$, with high strength and stiffness, enabling minimal deformation upon contact. The soft shell, representing the cement paste, surrounds the core with a thickness W_m, and exhibits lower strength and stiffness, permitting greater deformation or overlap.

The hard core typically employs a basic linear or nonlinear constitutive model to simulate the behavior of particles under

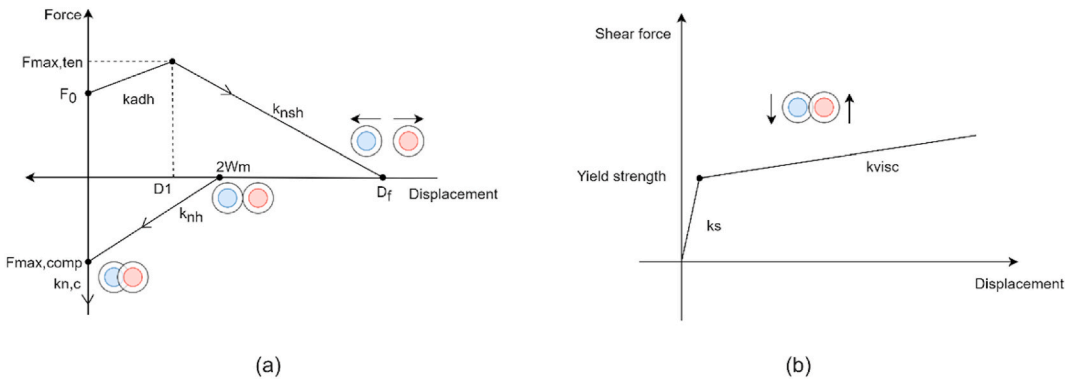

Fig. 4. Illustration of constitutive law: (a) normal contact, and (b) shear contact.

substantial compressive forces. Meanwhile, the soft shell represents the rheological properties of the concrete and is used to model particle failure under tensile or shear stress. The PFC library includes only basic constitutive relationships for particle interactions, which are inadequate for accurately simulating the rheological behavior of two-phase fresh concrete. To address this limitation, a custom-designed model was developed and the necessary constitutive relations using a user-defined function (UDF) were implemented, for both the normal and shear contacts, as illustrated in Fig. 4.

The force-displacement relationship for normal contact is depicted in Fig. 4 (a), illustrating the four stages that particles undergo under force: yielding, hardening, tension, and compression. Initially, in the yielding stage, particles undergo tensile forces with an overlap of less than W_m, leading the inter-particle force to reach the tensile yield strength F_0. As the particles enter the hardening stage, the distance between them increases until it reaches D_1 (see Fig. 4), determined by Eq. (3), at which point the maximum tensile force $F_{max,ten}$ is reached [32]. When it reaches the failure distance D_f, calculated by Eq. (4), the tensile force drops to zero [33]. During the compression stage, the particles are subjected to compressive forces, reducing the distance until they return to twice the soft-shell thickness (2 W_m), where contact is re-established. The force then gradually increases until the overlap equals W_m, at which point the compressive force $F_{max,comp}$ is reached. The force $F_{max,comp}$ is determined based on the stress distribution derived from slump test results. In theory, the tensile force $F_{max,ten}$ equals to $F_{max,comp}$ (see Fig. 4). Due to the high stiffness $k_{n,c}$ of the hard core, the force continues to increase along the y-axis under sustained compressive loading.

$$D_1 = 0.0375 \times \min(\tau_0 + 9, 18)\frac{V_{lip}}{r^3} \tag{3}$$

$$D_f = (1 + 0.5\,\varnothing)\sqrt[3]{\frac{V_{lip}}{r^3}} \tag{4}$$

where τ_0 is the shear yield stress, V_{lip} is the liquid volume, r is the particle radius, and $\varnothing$ is the contact angle.

The tangential force-displacement relationship, as illustrated in Fig. 4 (b), is divided into elastic and plastic stages. Initially, there is a phase of elastic deformation before the material reaches its yield strength. Upon reaching this yield strength, the particles transition into the plastic stage, where shear flow occurs, and plastic viscosity k_{vsic} becomes the dominant factor affecting energy dissipation.

3.3. Numerical models

3.3.1. Slump tests

The numerical model for slump tests is created, as shown in Fig. 5 (a). Stress distribution is predicted through slump tests, which are used to derive plastic viscosity from yield stress and subsequently adjust model parameters [26]. It is assumed that lifting the slump cone does not deform the concrete, there is no friction between the concrete and the horizontal surface, and the initial shape of the concrete is an ideal frustum. At a height where the cone is not yet lifted, the stress on the material exceeds the yield stress τ_0, causing the material below this point to continue flowing until the stress at this point reduces to the yield stress. Above the yield region, the shear stress does not exceed the yield stress, and this region remains undeformed. The final shape of the concrete consists of a deformed section and an undeformed section. Thus, the yield stress obtained from rheological experiments and the stress distribution from the slump test can be used to determine the normal force $F_{max,comp}$.

The calibration procedure followed in this study consists of four steps. First, the given input parameter, shear yield stress τ_0, is introduced into Eq. (5) to determine the height of the horizontal concrete layer in the cone. Second, the height from the base of the cone is identified, where the shear stress matches the specified yield stress. Third, a numerical simulation of the slump test is conducted, using a chosen set of basic model parameters (refer to Ref. [26]) and computing the distribution of normal compressive forces at various heights within the cone. Connecting these normal compressive forces across different heights should produce a curve that closely mirrors the analytically derived stress distribution. Fourth, the average normal contact stress for each 10 mm height interval is obtained. At the height corresponding to the shear yield stress identified in the first step, the average maximum compressive force between particles reflects the average normal contact force $F_{max,comp}$ associated with the yield stress (see Fig. 7).

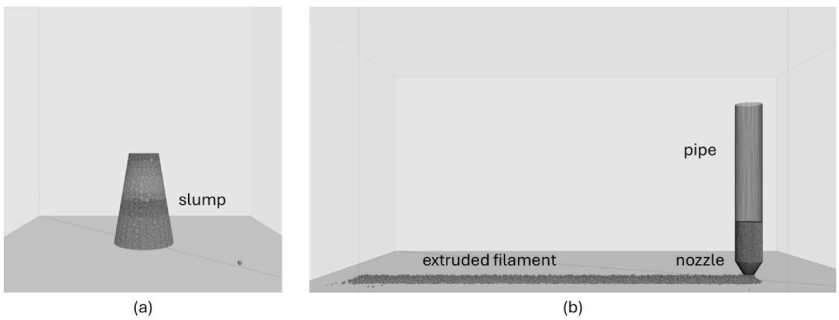

Fig. 5. Numerical model of (a) slump tests, and (b) 3D printing tests.

$$\tau_z = \frac{\rho g}{6} \cdot \frac{(H - Z)}{r_z^2} \cdot \left(r_z^2 + r_z r_t + r_t^2\right) \quad (5)$$

where r_t is the top radius of the cone, r_z is the radius of the cone at height Z, H is the total height of the cone, ρ is the volumetric mass density of the concrete, and g is the acceleration due to gravity [26].

Specifically, the process of creating the numerical model of slump tests involves four main steps. The first step is to define the cone geometry and boundary conditions, ensuring all model components are placed within this domain. Equipment such as the testing platform and slump cone are modeled with wall elements, as indicated in Fig. 3 (b). These walls, with shear and normal stiffness both set at 1×10^{10} N/m, a viscous coefficient of 0.2, a friction coefficient of 0.05, and a gravity of 9.81 m/s^2, interact only with particles (refer to Ref. [26]). The second step is to set up particle interactions. The third step is to model the fresh concrete as a cluster of two-phase particles with certain considerations, including the required concrete volume, particle size distribution, and spatial arrangement. Two-phase discrete particles are generated randomly, allowing them to settle under gravity until equilibrium, targeting an average unbalanced forces ratio of 1×10^{-5} and adjusting porosity to 0.1 by adding or removing particles. The last step is to define the motion of the slump cone to move vertically at 0.06 m/s for 5 s to stabilize the concrete particles.

3.3.2. 3D printing tests

The numerical model for 3D printing tests is shown in Fig. 5 (b). The procedure is the same as that of slump tests. The preparation process begins with randomly distributing two-phase particles throughout the entire volume, including the pipe and nozzle. This is accomplished using a random sequential addition generation algorithm, ensuring no overlap with previously placed particles [34]. To prevent material flow during preparation, a horizontal plane is placed at the bottom opening. After achieving equilibrium, a horizontal plane, moving vertically at a constant velocity of 15 mm/s, is positioned at the top of the material. This plane applies a confining pressure as the material begins to extrude from the nozzle. During extrusion, the material settles on a horizontal plane moving at a constant velocity of 20 mm/s. The pressure is recorded accordingly.

To compare the numerical simulation results with experimental results, detailed information about the shape of the simulated concrete specimen is required. In the numerical simulation, the shape of the contour is represented by a width expansion diagram. However, since the model concrete consists of discrete particles, all particles within a specified area must be scanned to locate the particle at the farthest distance. To achieve this, the entire free surface of the simulated concrete (the simulation domain) is divided into sectors, and each sector is scanned to find the particle with the maximum width coordinate in relation to the flow direction. After identifying and marking the widest particle within the respective sector, its position and width information is saved to a data file. In the next step, a cross-section is selected, and the contour shape corresponding to that cross-section is established. Since the program for obtaining the simulated concrete shape can be used at any time during the simulation process, the shape change can be monitored as a dynamic process.

4. Results

4.1. Experimental results

The results of rheological tests (static yield stress, dynamic yield stress, and plastic viscosity) and slump tests (slump and slump flow values) are shown in Table 2. The data reveals a clear relationship between the fineness modulus of the material and its rheological properties. As the fineness modulus decreases from 3.3 (the mixture M1) to 2.5 (the mixture M3), both the static and dynamic yield stresses, as well as plastic viscosity, decrease. Specifically, the static yield stress drops from 1118.7 Pa to 999 Pa, while the dynamic yield stress reduces from 338.8 Pa to 290.4 Pa. Similarly, plastic viscosity decreases from 139 Pa · s to 90 Pa · s. Similar results are also observed for the slump and slump flow values. This suggests that finer particles, indicated by a lower fineness modulus, result in a material that is easier to initiate flow, maintain flow under stress, and requires less energy to do so, making it more suitable for applications requiring high fluidity [35,36].

4.2. Simulation of slump tests

The rheological properties of the three mixtures are used as input parameters to calibrate the model through modeling slump tests. The spatial distribution of particles in the numerical model of slump tests is shown in Fig. 6. For slump (S), the relative error between experimental and simulated values varies across the mixtures. Mixture M1 shows the highest relative error at 14.1 %, with the experimental slump of 140 mm being lower than the simulated value of 163 mm. Furthermore, mixtures M2 and M3 exhibit relative errors of 3.7 % and 5.9 %, respectively. Regarding slump flow (SF), the relative errors are generally smaller compared to those

Table 2
Experimental results of rheological and slump tests.

No.	Static yield stress (Pa)	Dynamic yield stress (Pa)	Plastic viscosity (Pa · s)	Slump (mm)	Slump flow (mm)
M1	1118.7	338.8	139.0	140	230
M2	1070.5	319.8	93.7	155	270
M3	999.0	290.4	90.0	160	275

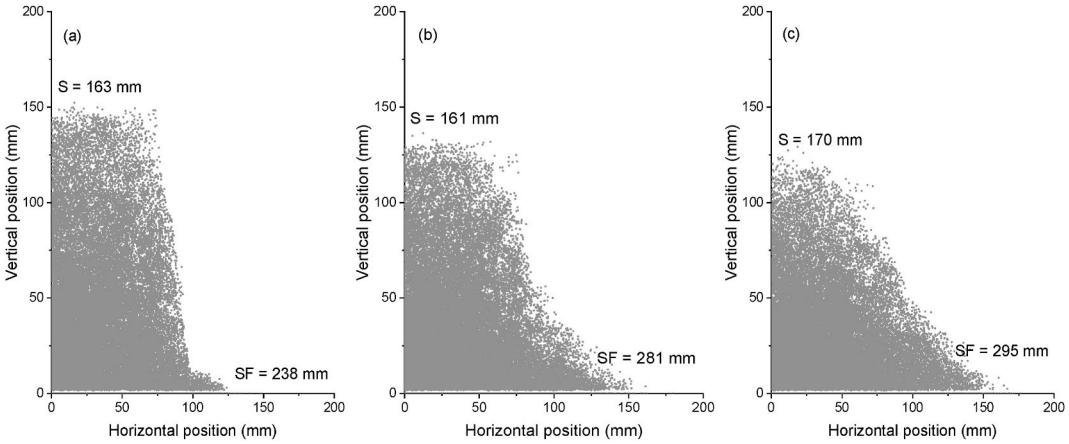

Fig. 6. Spatial distribution of particles in slump tests: (a) M1, (b) M2, and (c) M3.

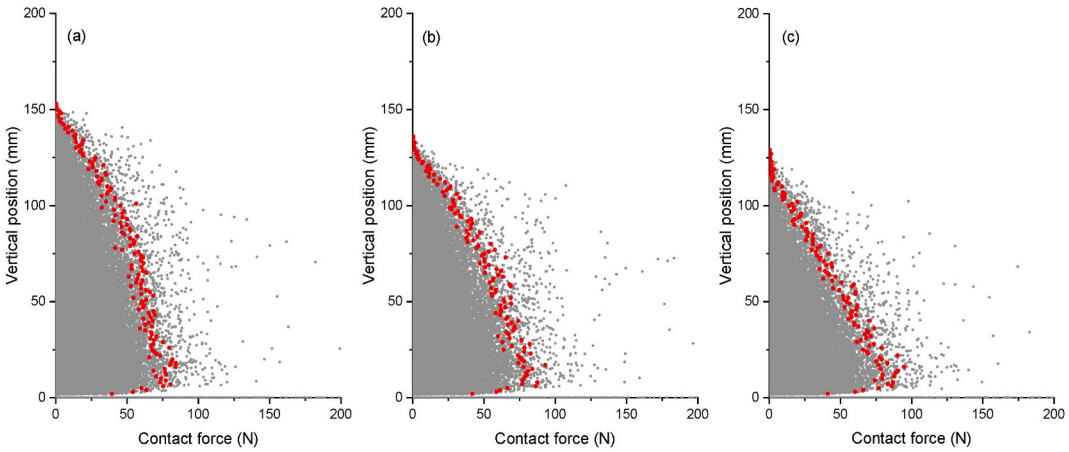

Fig. 7. Contact force of particles in slump tests: (a) M1, (b) M2, and (c) M3.

observed for slump. Mixture M1 shows a relative error of 3.4 %, with an experimental slump flow of 230 mm compared to a simulated value of 238 mm. Similarly, M2 and M3 exhibit relative errors of 3.9 % and 6.8 %, respectively, which are primarily due to minor settlements caused by compaction. While the errors for M2 and M3 are slightly higher than M1, they are still within an acceptable range, suggesting that the simulation model is fairly accurate in predicting the slump tests.

As described in Section 3.3.1, determining the normal contact force is a prerequisite for defining the constitutive law. The distribution of normal contact forces between particles along the slump height for the three mixtures is shown in Fig. 7. The red dots in the figure represent the average normal contact force at certain height intervals, specifically the average contact force of the highest 10 points. With the height values determined using Eq. (5), the average normal contact force can be obtained at the height corresponding to the shear yield stress.

4.3. Filament morphology

The morphology of extruded filaments obtained from both numerical simulation and experiments is shown in Fig. 8. The numerical simulation results of the mixture M1 indicate that when the ratio “a” (nozzle outlet diameter/maximum aggregate size) is smaller than 4, blockages occur during printing, with some particles being extruded from the nozzle, leading to discontinuous filaments. When the ratio “a” reaches 4, there is no (or limited) blockage as particles flow through the nozzle smoothly, resulting in consistent filament. For example, the M1-D5 group has a smooth extrusion process and a uniform distribution. However, when the ratio exceeds 5, the average filament width exceeds 50 mm (without considering the first and last 10 mm), causing over-extrusion and inadequate support in subsequent steps. For the mixture M2 with a fineness modulus of 2.9, consistent with the observations for the mixture M1, blockages occur during extrusion when the ratio “a” is smaller than 4. Compared to the mixture M1, the extruded filament width for M2 increases as the fineness modulus decreases. Additionally, when the ratio “a” is higher than 5, the lack of constraint from the nozzle causes the particles to fall due to gravity, resulting in an enlarged cross-section at the end (same as the mixture M1). In addition, the mixture M3

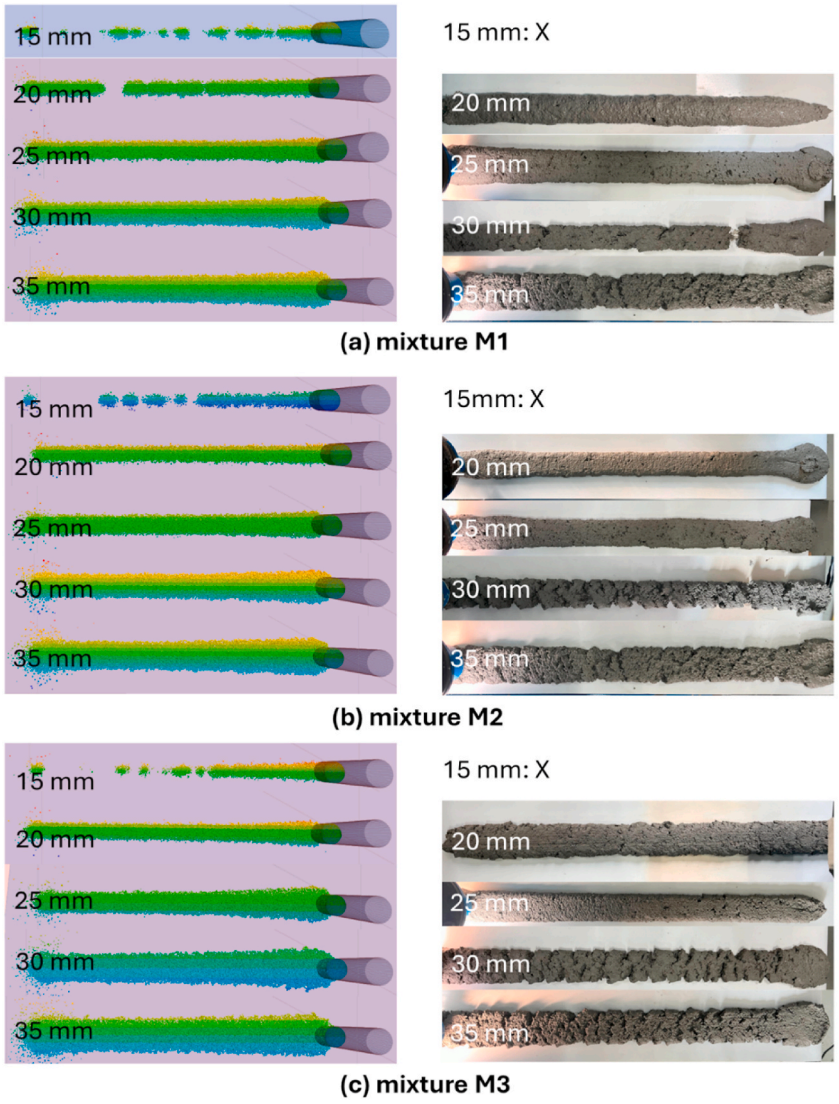

Fig. 8. Filament morphology: (a) M1, (b) M2, and (c) M3. Left side shows numerical simulation results, and right side shows experimental results. All mixtures are not extrudable using a nozzle with 15 mm diameter, i.e., M1-D3, M2-D3, and M3-D3, as indicated with "X".

with a fineness modulus of 2.5 is also presented. It is observed that the filament widths of M3-D6 and M3-D7 exceed 80 mm when the ratio "a" is higher than 5.

Regarding the experimental results of the extrusion tests varying the nozzle diameter, results show that when the ratio "a" is 3, blockages occurred for all three mixtures M1, M2, and M3 (indicated as X in Fig. 8). Note that the value "a" is influenced by multiple factors, such as the fineness modulus of the aggregates and the rheological properties of the paste. In cases where a higher fluidity is achieved by adjusting the mixture design, particularly using superplasticizers, the forces acting on particles - and thus the likelihood of clogging - can be reduced. When the ratio is 4, the extruded concrete filaments are homogeneous and smooth, with no interruptions or cracking during printing. The extrusion width remains stable and uniform at approximately 30 mm, closely matching the nozzle diameter, which indicates good extrudability. However, with the increase of the nozzle outlet diameter, the surface of 3D-printed concrete is prone to discontinuities. When the ratio "a" equals 5, surface quality and noticeable cracks in the extruded filaments are observed. For example, M1-D6 experienced extrusion fractures, and M1-D7 exhibited necking phenomena, while other groups showed varying degrees of edge warping. This is mainly due to changes in the material's flow characteristics within the nozzle. As the nozzle diameter increases, the flow rate of the concrete material at the nozzle center becomes relatively higher, while the flow rate near the inner walls of the nozzle is lower, leading to uneven material distribution. Additionally, the larger nozzle size reduces the extrusion force, resulting in insufficient material filling and the formation of larger voids. These factors contribute to the appearance of cracks, layers, or other discontinuities on the surface of the extruded concrete.

Despite some discrepancies in flowability, the developed two-phase discrete element model of 3D-printed filaments can reflect the

experimental results in terms of morphology in general. The simulations effectively capture the key geometric features of the extruded filaments. This alignment between simulated and experimental shapes indicates that the model provides a reliable representation of how the printed material conforms to the nozzle and builds up during the extrusion process.

The comparison between simulated and experimental widths of extruded filaments with varying nozzle diameters is shown in Fig. 9. As depicted in the figure, both the measured and simulated widths of the extruded filaments increase with the increase in nozzle diameter. Notably, the width variation for the mixture M3 is more pronounced, attributed to the use of more small-size aggregates and higher flowability accordingly. In addition, it was observed that the filament width obtained from numerical simulations tends to be higher than that from the extrusion experiments. When the ratio "a" (the nozzle diameter relative to aggregate size) is 4, the difference between the numerical and experimental results is less than 5 %. However, as the ratio increases, this discrepancy grows. For instance, when the ratio reaches 7, the difference rises to 45 % for mixture M3 and 32 % for mixture M1. This divergence can be attributed to the fact that at a ratio of 4, the extruded filament remains consistent and intact, while at higher ratios, cracks develop within the filament, leading to variations in layer width, as previously analyzed. Another reason may be that the two-phase discrete element model does not fully capture the complex interactions and behaviors of the materials during extrusion, leading to an overestimation of flowability in simulations. One possible avenue for improving the model's accuracy is by adjusting the viscous or friction coefficients to better reflect real-world conditions. This calibration, based on the extrusion simulation results, is an area for future investigation to enhance the predictive capability of the model and improve its alignment with experimental outcomes.

4.4. Extrusion pressure

Figs. 10 and 11 show the effect of the ratio "a" and the fineness modulus of aggregates on the extrusion force for the concrete mixtures based on numerical simulations and experiments, respectively. The results indicate that for all test groups, the extrusion force decreases as the ratio "a" increases. When the ratio "a" is less than 4, clogging occurs, and the extrusion force curve shows a steep incline. When the ratio is equal to or larger than 4, the extrusion force increases slowly. For example, for the mixture M1, the extrusion force is merely 17.4 N at 15 s when the ratio "a" is 7, while the value reaches 175.2 N at the same time when the ratio "a" is 3 from numerical results. A comparison between extrusion pressures at 15 s from both numerical simulations and experimental results was conducted. For the mixture M1, the pressure difference is 20 %, 16 %, and 55 % for ratios 5, 6, and 7, respectively. Despite the relatively large pressure difference for ratio 7, this can be considered acceptable due to the low overall pressure observed in both cases. The values for ratios 5 and 6 demonstrate that the model provides a reasonably accurate prediction when the material flows smoothly. However, a significant discrepancy arises for ratio 3, where the experimental pressure rapidly exceeds 200 N within a few seconds, whereas the simulation shows a more gradual pressure increase. This large difference can be attributed to the fact that at lower ratios, clogging or restricted flow is more likely to occur in the experiment, resulting in a sudden spike in pressure. In contrast, the numerical model, which assumes smoother flow conditions, may not fully capture the rapid clogging dynamics under these conditions. Improvements in the model could be achieved by incorporating more accurate representations of the material's rheological behavior under high-stress conditions, such as particle interactions and flow resistance in tight geometries, which is critical for predicting extrusion pressure in clog-prone scenarios.

During the clogging process, the top surface moves vertically, applying a vertical force on the particles. The normal pressure from the top surface increases the interactions between the solid particles, leading to the overlapping of the soft shells of the concrete particles and generating a significant reactive force on the bottom nozzle. Consequently, the extrusion force rises with the displacement of the top surface. However, when the ratio "a" is 4 or higher, although the top surface still applies normal pressure on the particles, the nozzle opening is sufficiently large to allow smooth extrusion without clogging. Therefore, the vertical force applied to the nozzle becomes negligible, and the solid particles do not overlap.

For the same ratio "a", the extrusion force decreases with a reduction in the fineness modulus, which corresponds to an increase in the cement paste. This decrease occurs because the extrusion force is primarily caused by the overlapping of coarse particles and

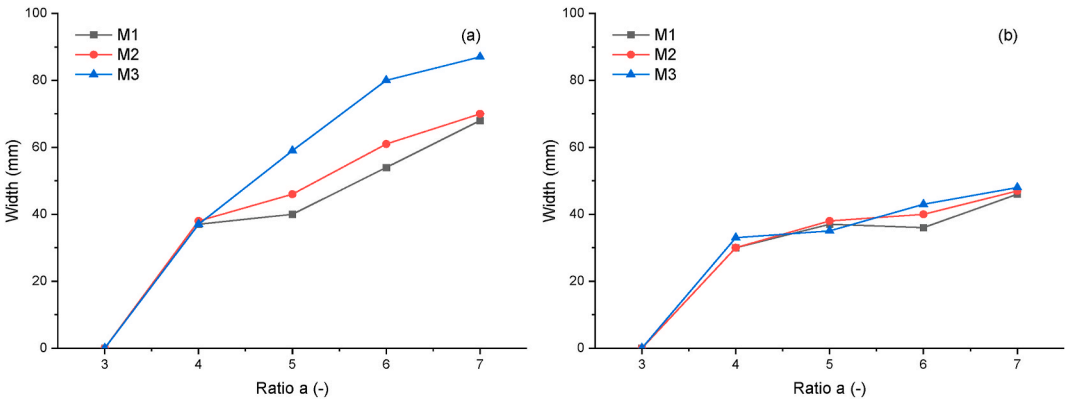

Fig. 9. Comparison of filament width: (a) numerical simulation, and (b) experimental results.

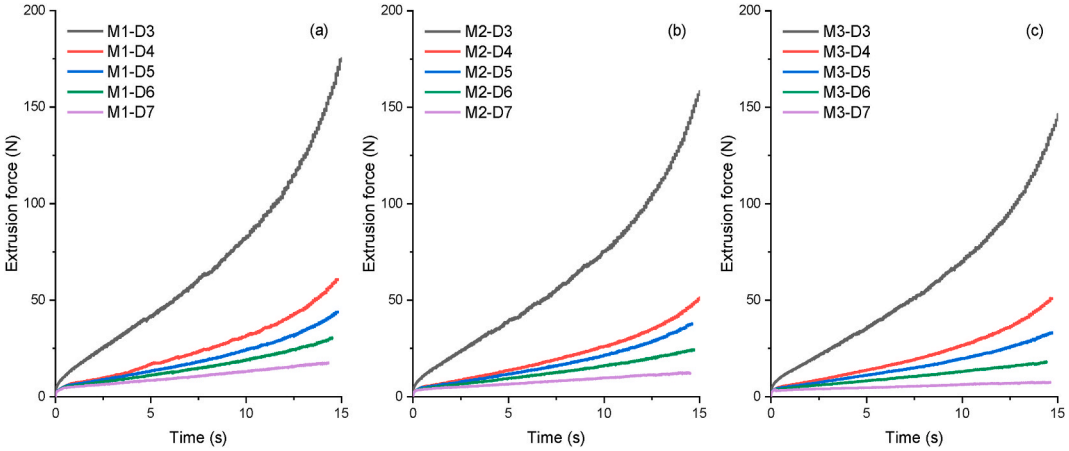

Fig. 10. Extrusion pressure from simulation: (a) M1, (b) M2, and (c) M3.

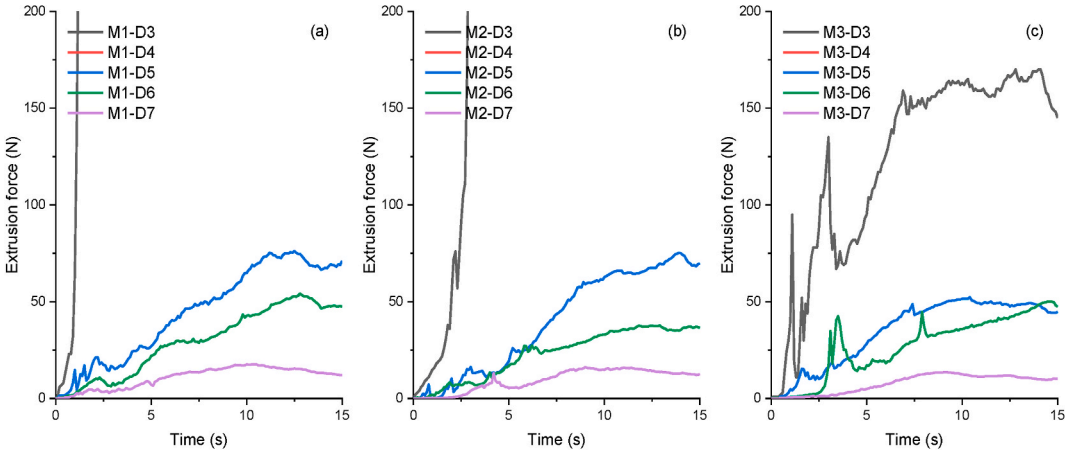

Fig. 11. Extrusion pressure from experiments: (a) M1, (b) M2, and (c) M3. Note the extrusion force of the series using the nozzle with a diameter of 20 mm was not successfully measured.

spheres forming the nozzle. Under clogging conditions, the extrusion force is mainly influenced by the contact between solid particles, with the interactions between hard-core particles being the primary reason for the extrusion force. In non-clogging conditions, the extrusion force is affected by the interactions between soft-shell particles and the nozzle. As the volume of the cement paste increases, the frictional force decreases, leading to a reduction in the extrusion force.

5. Discussion

The two-phase discrete element model offers significant potential compared to other modeling techniques for simulating the flow of fresh concrete. This is primarily because it accurately captures the discrete nature of concrete while also considering the rheological behavior of the paste. Such a combination makes the two-phase DEM a powerful tool for describing the flow of fresh concrete, provided the model is calibrated properly. However, several limitations remain, which require careful attention.

One key limitation is the reliance on describing fresh concrete as a collection of discrete particles. This approach introduces a range of parameters, particularly related to particle-particle and particle-wall interactions, that are not easily determined experimentally. As a result, many assumptions must be made, which underscores the need for meticulous calibration of these unknown parameters. Without this calibration, the predictive accuracy of the model may be compromised.

Another limitation pertains to the representation of aggregate particles. In this study, aggregates are modeled as spherical particles, which is an approximation. While this assumption can adequately represent certain aspects of the aggregates, it is not entirely accurate, especially for materials like manufactured sand, where particles exhibit irregular shapes. The irregularity increases the friction between particles and heightens the likelihood of clogging. As previously investigated by Tao et al. [37], the rheological properties of fresh concrete can be significantly influenced by changes in aggregate shape, and this needs to be considered in future refinements of the model.

Additionally, the model currently assumes constant rheological behavior, which does not fully account for the time-dependent properties of fresh concrete. Future studies should explore the incorporation of time-dependent behavior, especially in systems like 1K and 2K printing processes, where accelerators or other activators are introduced during extrusion. This rapid modification of rheological properties can alter the interactions between particles and potentially affect clogging behavior. To simulate this accurately, it is essential to test the evolution of rheological properties over time [38] and carefully calibrate the model's constitutive laws to reflect these rapid changes.

A further challenge relates to the issue of clogging due to fouling, a phenomenon driven by fast hydration. Fouling refers to the gradual accumulation and adhesion of the material to the internal surfaces of the extrusion nozzle or walls, exacerbating the clogging risk. Fast-setting materials are more prone to fouling, as they tend to accumulate more readily. The critical aspect here is to accurately define the interaction between particles and the walls, as well as particle clustering. Understanding and modeling these behaviors present additional challenges that require further investigation, particularly in the context of rapidly setting materials used in 3D concrete printing.

6. Conclusions and perspectives

This study explores the issue of extrudability in 3D concrete printing by utilizing both experimental and simulation methods. Three mixtures with different fineness modulus (2.5, 2.9, and 3.3) and five nozzles with varying outlet diameters (15, 20, 25, 30, and 35 mm) were used. A two-phase discrete element model was developed to simulate the concrete flow, treating it as a composite material consisting of two distinct phases: a rigid core representing the solid aggregate particles and a soft outer layer simulating the surrounding cement paste. Based on both the numerical and experimental results, the following conclusions can be drawn.

(1) A comparison between the numerical and experimental results of slump and slump flow values shows a maximum relative error of 14.1 %. This demonstrates that the simulation model is reasonably accurate in predicting slump behavior and can effectively capture key aspects of the rheological properties of fresh concrete. Despite the inherent complexities of concrete flow, the model's reliability is evident in its alignment with experimental data.
(2) The study also highlights that concrete with finer particles, characterized by a lower fineness modulus, is more efficient in initiating and maintaining flow under stress. These finer particles reduce the energy required for flow, which is advantageous in extrusion processes where smooth flow and low energy consumption are critical. A lower fineness modulus also reduces extrusion force, improving filament width consistency, and resulting in a steadier extrusion process with minimal variation.
(3) Both numerical simulations and experiments indicate that the morphology of extruded filaments is significantly influenced by the nozzle diameter-to-aggregate size ratio. When this ratio exceeds 4, the extrusion process is smooth and clog-free. However, ratios below 4 lead to clogging, with some particles causing discontinuous filaments as they are forced through the nozzle. In addition, the extrusion force increases more than 10 times when clogging occurs.
(4) While the two-phase discrete element model proves effective in analyzing clogging during the extrusion process, further refinement is necessary. Key areas for improvement include better modeling of particle shape, incorporating time-dependent rheology, and addressing fouling mechanisms. These advancements will make the model more robust and applicable to real-world 3D concrete printing scenarios.

CRediT authorship contribution statement

Yubo Sun: Writing – review & editing, Writing – original draft, Investigation. **Xinyue Zhang:** Writing – review & editing, Investigation. **Jiangang Zhou:** Writing – review & editing, Investigation. **Yilin Wang:** Writing – review & editing, Methodology, Conceptualization. **Bo Zhang:** Methodology, Investigation, Conceptualization. **Yiyuan Zhang:** Conceptualization, Data curation, Funding acquisition, Supervision, Validation, Writing – review & editing. **Weijiu Cui:** Writing – review & editing, Funding acquisition, Conceptualization. **Yaxin Tao:** Writing – original draft, Investigation, Funding acquisition.

Declaration of competing interest

The authors declare that they have no known competing financial interests or personal relationships that could have appeared to influence the work reported in this paper.

Acknowledgments

The authors acknowledge the financial support provided by the National Natural Science Foundation of China (Nos. 52008224), the Open Fund of the Institute for Sustainable Marine Architecture Research and Technological Innovation (iSMART) of Qingdao University of Science and Technology (Nu. 2020-031), the Key Technology Research and Development Program of Shandong Province (grant number 2019GSF110004), and the ETH Zurich Postdoctoral Fellowship (23-2 FEL-059).

Data availability

Data will be made available on request.

References

[1] K. Zhang, P. Chermprayong, F. Xiao, D. Tzoumanikas, B. Dams, S. Kay, B.B. Kocer, A. Burns, L. Orr, C. Choi, D.D. Darekar, W. Li, S. Hirschmann, V. Soana, S. A. Ngah, S. Sareh, A. Choubey, L. Margheri, V.M. Pawar, R.J. Ball, C. Williams, P. Shepherd, S. Leutenegger, R. Stuart-Smith, M. Kovac, Aerial additive manufacturing with multiple autonomous robots, Nature 609 (2022) 709–717, https://doi.org/10.1038/s41586-022-04988-4.

[2] V. Mechtcherine, K. van Tittelboom, A. Kazemian, E. Kreiger, B. Nematollahi, V.N. Nerella, M. Santhanam, G. de Schutter, G. Van Zijl, D. Lowke, E. Ivaniuk, M. Taubert, F. Bos, A roadmap for quality control of hardening and hardened printed concrete, Cement Concr. Res. 157 (2022) 106800, https://doi.org/10.1016/j.cemconres.2022.106800.

[3] G. Ma, R. Buswell, W.R. Leal da Silva, L. Wang, J. Xu, S.Z. Jones, Technology readiness: a global snapshot of 3D concrete printing and the frontiers for development, Cement Concr. Res. 156 (2022) 106774, https://doi.org/10.1016/j.cemconres.2022.106774.

[4] E. Lloret-Fritschi, T. Wangler, L. Gebhard, J. Mata-Falcón, S. Mantellato, F. Scotto, J. Burger, A. Szabo, N. Ruffray, L. Reiter, F. Boscaro, W. Kaufmann, M. Kohler, F. Gramazio, R. Flatt, From smart dynamic casting to a growing family of digital casting systems, Cement Concr. Res. 134 (2020) 106071, https://doi.org/10.1016/j.cemconres.2020.106071.

[5] M.K. Mohan, A.V. Rahul, K. Van Tittelboom, G. De Schutter, Rheological and pumping behaviour of 3D printable cementitious materials with varying aggregate content, Cement Concr. Res. 139 (2021) 106258, https://doi.org/10.1016/j.cemconres.2020.106258.

[6] M.K. Mohan, A.V. Rahul, G. De Schutter, K. Van Tittelboom, Early age hydration, rheology and pumping characteristics of CSA cement-based 3D printable concrete, Construct. Build. Mater. 275 (2021) 122136, https://doi.org/10.1016/j.conbuildmat.2020.122136.

[7] R.S. Teixeira, S.F.d. Santos, A.L. Christoforo, H. Savastano Jr., F.A.R. Lahr, Extrudability of cement-based composites reinforced with curauá (Ananas erectifolius) or polypropylene fibers, Construct. Build. Mater. 205 (2019) 97–110, https://doi.org/10.1016/j.conbuildmat.2019.02.010.

[8] V.N. Nerella, M. Näther, A. Iqbal, M. Butler, V. Mechtcherine, Inline quantification of extrudability of cementitious materials for digital construction, Cem. Concr. Comps. 95 (2019) 260–270, https://doi.org/10.1016/j.cemconcomp.2018.09.015.

[9] Y. Chen, Z. Li, S. Chaves Figueiredo, O. Çopuroğlu, F. Veer, E. Schlangen, Limestone and calcined clay-based sustainable cementitious materials for 3D concrete printing: a fundamental study of extrudability and early-age strength development, Appl. Sci. 9 (2019) 1809, https://doi.org/10.3390/app9091809.

[10] T. Wangler, R. Pileggi, S. Gürel, R.J. Flatt, A chemical process engineering look at digital concrete processes: critical step design, inline mixing, and scaleup, Cement Concr. Res. 155 (2022) 106782, https://doi.org/10.1016/j.cemconres.2022.106782.

[11] J. Kruger, G. van Zijl, A compendious review on lack-of-fusion in digital concrete fabrication, Addit. Manuf. 37 (2021) 101654, https://doi.org/10.1016/j.addma.2020.101654.

[12] X. Nan, Z. Wang, J. Hou, Y. Tong, B. Li, Clogging mechanism of pervious concrete: from experiments to CFD-DEM simulations, Construct. Build. Mater. 270 (2021) 121422, https://doi.org/10.1016/j.conbuildmat.2020.121422.

[13] D. Feys, G. De Schutter, S. Fataei, N.S. Martys, V. Mechtcherine, Pumping of concrete: understanding a common placement method with lots of challenges, Cement Concr. Res. 154 (2022) 106720, https://doi.org/10.1016/j.cemconres.2022.106720.

[14] G. De Schutter, D. Feys, Pumping of fresh concrete: insights and challenges, RILEM Tech, Letture 1 (2016) 76–80, https://doi.org/10.21809/rilemtechlett.2016.15.

[15] Y. Liu, L. Wang, Q. Yuan, J. Peng, Effect of coarse aggregate on printability and mechanical properties of 3D printed concrete, Construct. Build. Mater. 405 (2023) 133338, https://doi.org/10.1016/j.conbuildmat.2023.133338.

[16] S. Jacobsen, L. Haugan, T.A. Hammer, E. Kalogiannidis, Flow conditions of fresh mortar and concrete in different pipes, Cement Concr. Res. 39 (2009) 997–1006, https://doi.org/10.1016/j.cemconres.2009.07.005.

[17] N. Zhang, J. Sanjayan, Pumping-less 3D concrete printing using quick nozzle mixing, Autom. ConStruct. 166 (2024) 105609, https://doi.org/10.1016/j.autcon.2024.105609.

[18] R. Comminal, W.R. Leal da Silva, T.J. Andersen, H. Stang, J. Spangenberg, Modelling of 3D concrete printing based on computational fluid dynamics, Cement Concr. Res. 138 (2020) 106256, https://doi.org/10.1016/j.cemconres.2020.106256.

[19] M. Hosseinpoor, A. Yahia, K.H. Khayat, Modeling of flow performance of self-consolidating concrete using Dam Break Theory and computational fluid dynamics, Cem. Concr. Comps. 102 (2019) 14–27, https://doi.org/10.1016/j.cemconcomp.2019.04.018.

[20] N. Roussel, J. Spangenberg, J. Wallevik, R. Wolfs, Numerical simulations of concrete processing: from standard formative casting to additive manufacturing, Cement Concr. Res. 135 (2020) 106075, https://doi.org/10.1016/j.cemconres.2020.106075.

[21] H. Yu, W. Zhang, B. Yin, W. Sun, A. Akbar, Y. Zhang, K.M. Liew, Modeling extrusion process and layer deformation in 3D concrete printing via smoothed particle hydrodynamics, Comput. Methods Appl. Mech. Eng. 420 (2024) 116761, https://doi.org/10.1016/j.cma.2024.116761.

[22] T. Wang, F. Zhang, J. Furtney, B. Damjanac, A review of methods, applications and limitations for incorporating fluid flow in the discrete element method, J. Rock Mech. Geotech. Eng. 14 (2022) 1005–1024, https://doi.org/10.1016/j.jrmge.2021.10.015.

[23] T. Tavangar, M. Hosseinpoor, J.S. Marshall, A. Yahia, K.H. Khayat, Four-way CFD-DEM coupling to simulate concrete pipe flow: mechanism of formation of lubrication layer, Cement Concr. Res. 179 (2024) 107479, https://doi.org/10.1016/j.cemconres.2024.107479.

[24] Y. Liao, K. Cheng, W. Sun, Y. Zhao, Study on pumping wear characteristics of concrete pipeline based on CFD-DEM coupling, Sci. Rep. 13 (2023) 16119, https://doi.org/10.1038/s41598-023-42995-1.

[25] S. Remond, P. Pizette, A DEM hard-core soft-shell model for the simulation of concrete flow, Cement Concr. Res. 58 (2014) 169–178, https://doi.org/10.1016/j.cemconres.2014.01.022.

[26] V. Mechtcherine, S. Shyshko, Simulating the behaviour of fresh concrete with the Distinct Element Method – deriving model parameters related to the yield stress, Cem. Concr. Comps. 55 (2015) 81–90, https://doi.org/10.1016/j.cemconcomp.2014.08.004.

[27] X. Li, G. Xie, Z. Gao, C. Wang, A hard-core soft-shell model for vibration condition of fresh concrete based on low water-cement ratio concrete, Sci. Eng. Compos. Mater. 28 (2021) 689–701, https://doi.org/10.1515/secm-2021-0057.

[28] E. Ramyar, G. Cusatis, Discrete fresh concrete model for simulation of ordinary, self-consolidating, and printable concrete flow, J. Eng. Mech. 148 (2022) 04021142, https://doi.org/10.1061/(ASCE)EM.1943-7889.0002059.

[29] W. Cui, T. Wang, X. Chen, W. Shen, X. Shi, S. Wang, P. Zhang, Study of 3D printed concrete with low-carbon cementitious materials based on its rheological properties and mechanical performances, J. Sustain. Cement Based Mater. 12 (2023) 832–841, https://doi.org/10.1080/21650373.2023.2189172.

[30] Y. Tao, M.K. Mohan, A.V. Rahul, G. De Schutter, K. Van Tittelboom, Influence of rheology on mixing homogeneity and mechanical behavior of twin-pipe 3D printable concrete, Construct. Build. Mater. 408 (2023) 133694, https://doi.org/10.1016/j.conbuildmat.2023.133694.

[31] Y. Tao, J. Zhou, W. Cui, X. Shi, G. De Schutter, K. Van Tittelboom, Numerical assessment of plastic yielding in extrusion-based 3D concrete printing, Mater. Struct. 57 (2024) 65, https://doi.org/10.1617/s11527-024-02325-x.

[32] T. Mikami, H. Kamiya, M. Horio, Numerical simulation of cohesive powder behavior in a fluidized bed, Chem. Eng. Sci. 53 (1998) 1927–1940, https://doi.org/10.1016/S0009-2509(97)00325-4.

[33] K. Krenzer, V. Mechtcherine, U. Palzer, Simulating mixing processes of fresh concrete using the discrete element method (DEM) under consideration of water addition and changes in moisture distribution, Cement Concr. Res. 115 (2019) 274–282, https://doi.org/10.1016/j.cemconres.2018.05.012.

[34] K. El Cheikh, S. Rémond, N. Khalil, G. Aouad, Numerical and experimental studies of aggregate blocking in mortar extrusion, Construct. Build. Mater. 145 (2017) 452–463, https://doi.org/10.1016/j.conbuildmat.2017.04.032.

[35] N. Roussel, Understanding the Rheology of Concrete, Elsevier, 2011 0857095285.

[36] Q. Ren, Y. Tao, D. Jiao, G. De Schutter, Z. Jiang, Rheological properties of concrete with manufactured sand: a multi-level prediction, Cem. Concr. Comps. 133 (2022) 104647, https://doi.org/10.1016/j.cemconcomp.2022.104647.
[37] Y. Tao, Q. Ren, K. Lesage, K. Van Tittelboom, Y. Yuan, G. De Schutter, Shape stability of 3D printable concrete with river and manufactured sand characterized by squeeze flow, Cem. Concr. Comps. 133 (2022) 104674, https://doi.org/10.1016/j.cemconcomp.2022.104674.
[38] A.U. Rehman, I.-G. Kim, J.-H. Kim, Towards full automation in 3D concrete printing construction: development of an automated and inline sensor-printer integrated instrument for in-situ assessment of structural build-up and quality of concrete, Dev. Built Environ. 17 (2024) 100344, https://doi.org/10.1016/j.dibe.2024.100344.